Biochemistry and Biophysics Reports 37 (2024) 101649

Contents lists available at ScienceDirect

Biochemistry and Biophysics Reports

journal homepage: www.elsevier.com/locate/bbrep

Characterization of a catalase-peroxidase variant (L333V-KatG) identified in an INH-resistant *Mycobacterium tuberculosis* clinical isolate

Brenda Uribe-Vázquez [a,1], Adelaida Díaz-Vilchis [b,1], Aylin Avila-Linares [b], Gloria Saab-Rincón [a], Yerli Marín-Tovar [b], Humberto Flores [a], Nina Pastor [c], Guillermo Huerta-Miranda [a], Enrique Rudiño-Piñera [b], Xavier Soberón [a,*]

[a] Departamento de Ingeniería Celular y Biocatálisis, Instituto de Biotecnología, UNAM, Avenida Universidad 2001, Colonia Chamilpa, 62210, Cuernavaca, México
[b] Departamento de Medicina Molecular y Bioprocesos, Instituto de Biotecnología, UNAM, Avenida Universidad 2001, Colonia Chamilpa, 62210, Cuernavaca, México
[c] Centro de Investigación en Dinámica Celular, Instituto de Investigación en Ciencias Básicas y Aplicadas, UAEM, Avenida Universidad 1001, Colonia Chamilpa, 62209, Cuernavaca, Morelos, México

ARTICLE INFO

Keywords:
Catalase-peroxidase structure
Kinetics
KatG
Mycobacterium tuberculosis
L333V
Heme

ABSTRACT

Mycobacterium tuberculosis catalase-peroxidase (*Mt*-KatG) is a bifunctional heme-dependent enzyme that has been shown to activate isoniazid (INH), the widely used antibiotic against tuberculosis (TB). The L333V-KatG variant has been associated with INH resistance in clinical *M. tuberculosis* isolates from Mexico. To understand better the mechanisms of INH activation, its catalytic properties (catalase, peroxidase, and IN-NAD formation) and crystal structure were compared with those of the wild-type enzyme (WT-KatG). The rate of IN-NAD formation mediated by WT-KatG was 23% greater than L333V-KatG when INH concentration is varied. In contrast to WT-KatG, the crystal structure of the L333V-KatG variant has a perhydroxy modification of the indole nitrogen of W107 from MYW adduct. L333V-KatG shows most of the active site residues in a similar position to WT-KatG; only R418 is in the R-conformation instead of the double R and Y conformation present in WT-KatG. L333V-KatG shows a small displacement respect to WT-KatG in the helix from R385 to L404 towards the mutation site, an increase in length of the coordination bond between H270 and heme Fe, and a longer H-bond between proximal D381 and W321, compared to WT-KatG; these small displacements could explain the altered redox potential of the heme, and result in a less active and stable enzyme.

1. Introduction

Tuberculosis (TB) remains one of the top ten causes of death worldwide and the leading cause of death from a single infectious agent [1]. Worldwide, an estimated 10 million people fell ill with TB and 1.2 million TB deaths occurred among HIV-negative patients in 2019 [1]. The growing appearance, prevalence, and severity of drug-resistant TB has led to an increased interest to understand the fundamental molecular bases of resistance [2,3]. The most frequent instance of resistance is one of the most widely used and effective drugs for TB-treatment for over 60 years, isonicotinic acid hydrazide (isoniazid or INH); in 2019 there were an estimated 1.4 million cases of INH-resistant TB [1,3]. Catalase-peroxidases (KatGs) are involved in INH-resistance and have been the subject of intense scrutiny [4,5].

KatGs are heme-dependent oxidoreductase enzymes encoded by the *katG* gene found in bacteria and lower eukaryotes and are grouped as class I of the bacterial, fungal, and plant heme peroxidases superfamily, also known as the non-animal superfamily (the largest clade, in both prokaryotic and eukaryotic lineages, of heme peroxidases). They are named after their capability to perform both two-electron oxidation-reduction reactions involving two hydrogen peroxide (H_2O_2) molecules per cycle (catalase reaction) and one-electron oxidation of a wide range of aromatic compounds (peroxidase reaction). The robustness of the catalase reaction is comparable with that of monofunctional catalases even though KatG shares no structural homology with them [3,6–10]. Consequently, it has been proposed that the main role of these enzymes

Abbreviations: KatG, catalase-peroxidase; INH, isoniazid; TB, tuberculosis; InhA, long-chain enoyl acyl carrier protein reductase; CD, circular dichroism.

* Corresponding author. Departamento de Ingeniería Celular y Biocatálisis, Instituto de Biotecnología, UNAM, México, Avenida Universidad 2001, Colonia Chamilpa, 62210, Cuernavaca, México.
E-mail address: xavier.soberon@ibt.unam.mx (X. Soberón).

[1] Both authors contributed equally to this work.

https://doi.org/10.1016/j.bbrep.2024.101649
Received 23 October 2023; Received in revised form 24 December 2023; Accepted 15 January 2024

is to protect organisms (especially plant and animal pathogens) from toxic molecules, including H_2O_2 and H_2O_2-derived species like hydroxyl radical and hypochlorite produced by host defense systems [11,12].

The *Mycobacterium tuberculosis* KatG (*Mt*-KatG) has been subject of numerous studies due to its implication in resistance to INH [11,13]. It is known that KatG generates an isonicotinoyl radical, which subsequently reacts with NAD^+ to generate an IN-NAD covalent adduct. IN-NAD then inhibits the long-chain enoyl acyl carrier protein reductase (InhA), involved in the biosynthesis of mycolic acid, as part of the type II system of fatty acid biosynthesis that affords this major constituent of the cell wall (Fig. 1), inducing cell lysis [4,6,8,14]. Inhibition of InhA by the IN-NAD was clearly demonstrated when the crystal structure of InhA containing an IN-NAD was determined (PDB 2IDZ) [15]. Also, mutations in the InhA protein/*inhA* promoter either preventing the IN-NAD binding or overexpressing InhA are well understood [3,4,8,11,16]. However, the molecular basis of how mutations in the *katG* gene interfere in INH activation, the precise mechanism by which KatG forms the radical, and the mode of interaction of INH with KatG including the exact binding sites for INH (and, potentially, NAD^+), remain unclear and are the subjects of ongoing investigation [5,13,14,17].

There are seven basic structures of catalase-peroxidases deposited in the PDB databank (March 2023). *Haloarcula marismortui* KatG (*Hm*-KatG, PDB 1ITK), *Synechococcus elongatus* KatG (*Se*-KatG, PDB 1UB2), *Burkholderia pseudomallei* KatG (*Bp*-KatG, PDB 1MWV), *Escherichia coli* KatG C-domain (PDB 1U2J), *Magnaporthe grisea* KatG (PDB 3UT2), *Mt*-KatG (PDB 2CCA), and *Neurospora crassa* CAT-2 (PDB 5WHQ). Several other crystallographic structures have been published, including those of engineered versions with single amino acids replacements, at diverse pH values, of oxidized forms, and in complex with substrates [11]. A comparison of these structures shows a functional homodimer in which each monomer is composed of two mainly α-helical domains. The N-terminal domain contains the active site of the enzyme that includes a heme binding site surrounded by a proximal pocket (made up of H270, W321, and D381, *Mt*-KatG numbering) and a distal pocket (R104, W107, D137, and H108) (Fig. 2A); a unique structural feature to KatG enzymes are the covalent bonds bridging the amino acids W107, Y229, and M255 via their side chains in the distal pocket; the resulting adduct is required for the catalase but not the peroxidase activity. There is also an invariant R418, which has been postulated to act as a molecular switch modulating the redox properties of the M-Y-W adduct [4,6,11]. This mobile arginine is found in two conformations (the Y- and R-conformations); its interconversion is pH-dependent suggesting that it participates in the H_2O_2 dismutation reaction (Fig. 2A) [3,6,7]. The C-terminal domain is structurally similar to the N-terminal domain, concordant with the suggestion of a gene duplication event; however, this domain lacks a heme group. Heme KatG is solvent accessible where the distal heme pocket is connected to the outside of the protein through a narrow channel. This pocket is filled by a grid of organized water molecules and bordered by amino acid Ser315. This residue has been shown to bind one INH molecule (NIZ-1 in Fig. 2B) in the crystallographic structures of *Haloarcula marismortui* KatG enzyme in complex with INH (PDB 1ITK), and recently in *Mt*-KatG by cryogenic electron microscopy (PDB 7AG8). Other potential INH binding sites, although remote from the heme, have been reported in various KatGs enzymes, such as NIZ-1, NIZ-3 and NIZ-4 from *Se*-KatG and NIZ-2 from *Bp*-KatG (Fig. 2B) [4,6,11,14,16,17].

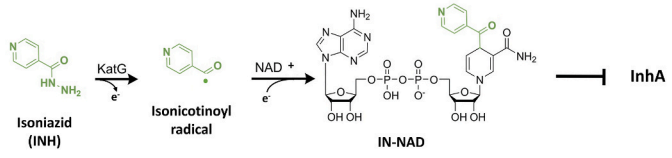

Fig. 1. The general INH mechanism of action. INH is activated by KatG to generate the IN-NAD adduct. The IN-NAD inhibits InhA. The inhibition results in stopping mycolic acid biosynthesis and, ultimately, cell death.

To shed light into the KatG properties and its interaction with INH, here we report the crystal structure of the L333V-KatG variant and its biochemical characterization. The *M. tuberculosis* strain containing this variant was first isolated at the National Institute of Respiratory Diseases (Mexico) and it was later reported in Veracruz [18], the state with the highest rate of TB in Mexico. It has never been reported outside Mexico, so it may represent a novel way to develop resistance to INH.

2. Materials and methods

2.1. Plasmid preparation and site-directed mutagenesis

To produce recombinant WT-KatG protein, the coding region of the *katG* gene was PCR amplified from an INH-sensitive clinical isolate with the primers katG 5′ H6 (5′ GAA ACA GAA TTC ATA TG**C ACC ATC ACC ATC ACC AT**C CCG AGC AAC ACC CA 3′) and katG 3’ (5′ AAA CAG AAG CTT CAG CGC ACG TCG AAC C 3′). The oligonucleotides incorporated an *Eco*RI restriction site at the 5′ end, a modification of the GTG start codon (translated as Valine) of the mycobacterium to ATG (Methionine), the introduction of a *Hind*III restriction site after the TGA stop codon, and the addition of a coding sequence for six His-tag (bold and underlined letters) at the 5′ end. The PCR product was cloned in the pKK-223-3 vector to produce plasmid pKK-WT-KatG.

Site-directed mutagenesis was performed to introduce the L333V change in the *katG* gene by the megaprimer method [19]. Plasmid pKK-WT-KatG was used as the template. Oligonucleotides L333V (5′ AGC CGT ACA GGA TCT CGA **C**GA AAC TGT TGT CCC ATT TC 3’) and pkk 5’ (5′ ATC ATC GGC TCG TAT AAT GTG TGG A 3′) were used in a first round of PCR. Bold and underlined letter in the sequence indicate the replaced nucleotide. This PCR product was used as a megaprimer to generate the full-length gene with the oligonucleotide pkk 3’ (5′ CGC CAG GCA AAT TCT GTT TTA TCA GAC CGC 3′) in a second round PCR. *Pfu* polymerase was used in all PCR amplifications. The PCR product (2223 bp fragment) was digested with restriction enzymes *Eco*RI and *Hind*III and ligated to the expression vector pKK-223-3 using *T4* DNA ligase to produce plasmid pKK-L333V-KatG.

The ligation product was introduced into MC1061 *Escherichia coli* strain cells by electroporation. Transformants were selected using ampicillin (200 μg/mL) containing Luria Broth (LB) agar plate media. Liquid cultures of LB-ampicillin were inoculated with individual colonies, grown overnight at 30 °C and centrifuged. Plasmid DNA was extracted and purified from the bacterial pellet using the High Pure Plasmid Isolation kit (Roche, Germany). Candidate plasmids were screened by *Eco*RI and *Hind*III restriction digestion. Positive candidates were sent for full *katG* gen DNA sequence analysis by the Sanger method (DNA synthesis and sequencing laboratory of Biotechnology Institute/UNAM, Mexico) to confirm that the correct modifications had been introduced without any unintended mutations.

2.2. Protein expression and purification

Following confirmation of the correct DNA sequence, the pKK-KatG plasmids (WT and L333V) were introduced by transformation into *E. coli* MC1061 *ΔbioH*/pREP4 cells. The cells were plated onto LB plates with 200 μg/mL of ampicillin and 25 μg/mL of kanamycin and grown overnight at 30 °C. Starter cultures (LB-ampicillin; 2 mL each) were inoculated with a single colony and grown overnight at 30 °C. Each starter culture was further used to inoculate 50 mL of LB medium supplemented with 200 μg/mL ampicillin and 30 mg/L hemin (dissolved in 0.2 N NaOH). To ensure stoichiometric incorporation of the heme cofactor during overexpression in *E. coli*, hemin was added to the medium [2]. Protein expression was then induced by the addition of 1 mM of isopropyl β-D-1- thiogalactopyranoside (IPTG) when the cultures had an OD_{600nm} of 0.6. Cells were grown for 4 h after induction and collected by centrifugation (5000 rpm for 20 min).

After centrifugation, the cell pellet was resuspended in 50 mM

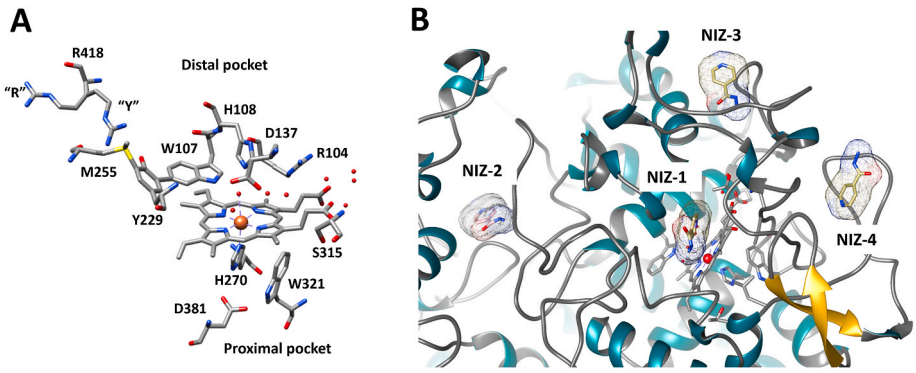

Fig. 2. A) Structural peculiarities of *Mt*-KatG active site, with the proximal and distal pockets. B) INH possible binding sites (NIZ) found in different KatGs; the Fe of the heme group is shown as a red sphere. (For interpretation of the references to colour in this figure legend, the reader is referred to the Web version of this article.)

Na_2HPO_4/NaH_2PO_4 buffer (pH 7.5). The suspension was mixed by vortexing and incubated at 4 °C for 30 min before sonication. Cells were lysed by sonication in an ice bucket with a Branson 450 ultrasonicator fit with a standard microtip set to constant output and 3.5 duty. Sonication was carried out in five cycles (20 s on, 40 s off). Insoluble material was removed by centrifugation at 10,000 rpm for 20 min at 4 °C, resulting in a viscous, red-brown crude extract.

The supernatant with the His-tagged KatG protein was purified in a 1 mL column of Ni-NTA agarose resin (Invitrogen, USA), following the manufacturer's instructions. Briefly, an initial step with water and Buffer 50 mM $NiSO_4$ was carried out. Subsequent washes were performed using buffer A (0.5 M NaCl and 50 mM Na_2HPO_4/NaH_2PO_4 pH 7.5) supplemented with 5 mM imidazole and then 35 mM imidazole. KatG proteins were then eluted using buffer A supplemented with 200 mM imidazole.

After elution from the resin, dialysis against 20 mM Na_2HPO_4/NaH_2PO_4 buffer (pH 7.5) was carried out overnight. Purified KatG was concentrated and desalted with Merck Amicon Ultra Centrifugal Filter. Protein concentration was determined using the Bradford method. All assays were performed in triplicate. Following purification, KatG showed a UV–visible spectrum indistinguishable from that previously reported [14]. The homogeneity of protein was determined by SDS-PAGE 10%.

2.3. Biochemical characterization

All assays were performed with minor modifications from published procedures [14] and were conducted at room temperature using UV–visible Beckman Coulter DU 730 spectrophotometer.

Catalase activity was evaluated spectrophotometrically by monitoring the decrease over 60 s (linear least-squares fittings) of the H_2O_2 initial concentrations (0.5, 1, 3, 6, 12, 20, and 25 mM) at 240 nm (ε240nm = 0.0435 mM^{-1} cm^{-1}) with a fixed KatG concentration of 30 nM. The reaction mixture contained 50 mM Na_2HPO_4/NaH_2PO_4 buffer (pH 7.5).

Peroxidase activity was determined by following the oxidation rate of *O*-dianisidine at 460 nm (ε460nm = 11.3 mM^{-1} cm^{-1}) with initial concentrations from 1.5 μM to 200 μM in the presence of 23 mM *tert*-butyl hydroperoxide (tBHP), 50 mM sodium acetate buffer (pH 5.5) and 100 nM KatG.

IN-NAD formation was assayed spectrophotometrically at 326 nm using the extinction coefficient ε326nm = 6,900 M^{-1} cm^{-1}. The reaction was carried out in 50 mM Na_2HPO_4/NaH_2PO_4 buffer (pH 7.5), using KatG (0.7–1 μM, depending on the variant concentration), in the presence of a constant flow of H_2O_2 generated by a glucose/glucose oxidase system (G/Gox), with concentrations of 16.7 mM and 66.6 mU/mL, respectively [20]. Apparent K_m values for INH were determined by using reaction mixtures containing initial concentrations of either INH (0.4, 0.8, 1.6, 3.2, 6.4, 12.8 and, 25.6 mM) with a constant concentration of NAD^+ (1 mM) and NAD^+ (30, 60, 120, 240, 480 and, 960 μM) with a constant concentration of INH (15 mM).

2.4. Circular dichroism spectropolarimetry (CD)

The thermal unfolding of KatG (WT and L333V) was monitored by Far-UV and Visible CD spectra. The loss of secondary structure was evaluated by the change in ellipticity at 222 nm, and the loss of tertiary contacts in the heme was followed at 410 nm during a temperature gradient from 20 to either 62 or 90 °C. The analysis in the far UV region was performed at protein concentrations between 0.3 and 0.6 mg/mL in 10 mM Na_2HPO_4/NaH_2PO_4 (pH 7.5). All spectra were recorded using a 715 Jasco spectropolarimeter. Far-UV spectra were recorded in a 1 mm quartz cell using this setup: 190–260 nm λ range, 1 nm data step, and 50 nm/min scan rate, averaging the signal for 8 s. Jasco J-720 spectrum software was used for baseline corrections and data analysis. The reversibility of the unfolding process was tested by decreasing the temperature from the final temperature to 20 °C at a 1 °C/min rate. Initial and final CD spectra were recorded. The CD heme spectra were recorded in a 1 cm quartz cell, at 20 °C with the following settings: λ range of 500-260 nm, continuous scan mode, a scan speed of 50 nm/min, data step of 1 nm, and with a protein concentration of 2 mg/mL. Each spectrum is the result of averaging the signal for 8 s and three scans. The apparent fraction of unfolded protein (Fapp) was estimated by normalizing the ellipticity at each temperature between the unfolded and native baseline signals.

2.5. X-ray crystallography

L333V-KatG crystals were obtained by the sitting-drop vapor-diffusion method at 18 °C. The drops were prepared with a Mosquito LCP (TTP Labtech) crystallization robot in 96-well IQ plates (TTP Labtech). Each (0.3 μL) drop contained the enzyme at 24 mg/mL, in 20 mM Na_2HPO_4/NaH_2PO_4 buffer, pH 7.5, and the crystallization solution (0.3 μL) containing 10% w/v PEG 6000 and 100 mM HEPES/Sodium Hydroxide, pH 7.0. Red-brown plate-like crystals were visible after 4 weeks and continued to grow for two months. Crystals were flash-cooled by immersion in liquid nitrogen exchanging water with 30% PEG 400 into the mother liquor as cryoprotectant. To formally compare the crystallographic structures the L333V-KatG variant and the WT-KatG enzyme, several unsuccessful attempts were made to obtain crystals of WT-KatG. Accordingly, we structurally compare L333V-KatG with WT-KatG previously reported at 2.0 Å resolution (PDB ID 2CCA) [5].

A diffraction data set was collected from a flash-cooled crystal at the 19ID beamline of the Advanced Photon Source, Argonne National Laboratory (Argonne, IL, U.S.A.) using a Pilatus 3X 6 M detector. Reflections were indexed, integrated, and scaled with the XDS package [21]. The L333V-KatG crystal belongs to the monoclinic space group $P2_1$ with cell dimensions a = 82.6, b = 150.8, c = 127.0 Å and β = 90.45°

(Supplementary Table S1).

Phases for the structure were determined by molecular replacement using the coordinates of the *M. tuberculosis* WT-KatG (PDB ID 2CCA) [5] as a starting model and performed with the program Phaser [22]. Phases were improved by rigid-body refinement and geometric constraint performed in REFMAC [23]. The final model was refined alternating cycles of automatic and manual refinement with PHENIX [24] and COOT [25], respectively, to a final R_{work} of 18.0% (R_{free} of 22.6% calculated with 5% of the data randomly selected) at 2.1 Å (Supplementary Table S1). The final crystallographic structure displayed good stereochemistry, as analyzed by MOLPROBITY [26]. Structural figures were made with the PyMOL Molecular Graphics, Version 1.8 Schrödinger, LLC. Coordinates and structure factors have been deposited in the Protein Data Bank (PDB ID 8DWR).

2.6. Electrochemical characterization

The electrochemical measurements were performed inside a glass three-electrode cell in an anaerobic atmosphere of N_2:CO_2 (80:20). Ag/AgCl was used as the reference electrode, a graphite rod as the counter electrode, and a platinum wire (Pt) as the working electrode. The protein was adsorbed on the Pt electrode by incubating the electrode in the protein solution overnight. The elution buffer was used as the electrolyte solution. Cyclic Voltammetry (CV) and Square Wave Voltammetry (SWV) were used in this study. All the potential values in this work are referred to the Standard Hydrogen Electrode (SHE = 0.199 V vs. Ag/AgCl). CV was performed in a potential window from −0.3 to 1.2 V at a 0.1 V/s scan rate. SWV was performed at a step potential of 0.001 V, 0.003 V modulation amplitude, and a frequency of 19 Hz. The scan started from positive to negative potentials in the same potential window as the CV.

3. Results and discussion

3.1. Protein purification

In the present study His-tag proteins (WT-KatG and L333V-KatG) were produced by the pKK-KatG expression system to overproduce the protein in *E. coli* MC1061 strain. The His6-tag was introduced to facilitate the purification of the protein by nickel affinity chromatography. The enzymes were characterized without removing the His-tag since it was reported not to affect the enzymatic properties [14]. The two proteins were obtained with typical yields of ~3 mg per 50 ml of culture for kinetic and spectroscopic experiments and ~20 mg per liter of culture for crystallography. They displayed a single band of ~80 kDa on SDS-PAGE.

3.2. Kinetic characterization

Recombinant WT-KatG and L333V-KatG were characterized kinetically using a combination of biochemical assays; we compared the catalase and peroxidase activities, and the IN-NAD adduct formation for different concentrations of both substrates, INH and NAD^+, which yielded different values for each variant (Table 1).

The apparent K_m and k_{cat} values of the WT-KatG were determined for the catalase (1.98 mM and 2200 s^{-1}, respectively) and peroxidase activity (2.11 μM and 6.4s^{-1}, respectively). These kinetic parameters agreed with previously reported values determined by HPLC and spectrophotometrically for WT-KatG, ranging K_m from 1 to 30 mM and k_{cat} from 2300 to 10,000 s^{-1} for catalase and K_m from 9 to 80 μM and k_{cat} from 0.2 to 30 s^{-1} for peroxidase [14,27–29].

The L333V-KatG variant displayed 40% and 33% of the catalase and peroxidase activity, respectively, relative to WT-KatG k_{cat}/K_m (Table 1). On the other hand, L333V-KatG retained significant capacity to form IN-NAD (k_{cat}/K_m), around 57% when INH concentration is varied. When NAD^+ concentration is varied, no significant changes were observed.

Table 1
Kinetic parameters comparison of three different enzymatic activities (catalase, peroxidase and IN-NAD formation for both substrates) for WT-KatG and the variant L333V-KatG.

Activity	Substrate	Kinetic parameter	WT-KatG	L333V-KatG
Catalase	H_2O_2	K_m (mM)	2.0 ± 0.5	2.3 ± 0.4
		k_{cat} (s^{-1})	2200 ± 134	1034 ± 45
		k_{cat}/K_m (M^{-1}/s^{-1})	1.1 x 10^6 ± 2.6 x 10^5	4.4 x 10^5 ± 1.1 x 10^5
Peroxidase	*O*-dianisidine	K_m (μM)	2.1 ± 0.8	1.6 ± 0.5
		k_{cat} (s^{-1})	6.4 ± 0.4	1.6 ± 0.1
		k_{cat}/K_m (M^{-1}/s^{-1})	3.1 x 10^6 ± 5.0 x 10^5	1.0 x 10^6 ± 1.7 x 10^5
IN-NAD formation	INH	K_m (mM)	1.9 ± 0.1	3.7 ± 0.3
		k_{cat} (s^{-1})	0.098 ± 0.001	0.107 ± 0.003
		k_{cat}/K_m (M^{-1}/s^{-1})	50.6 ± 14.2	28.8 ± 9.5
IN-NAD formation	NAD^+	K_m (μM)	210 ± 40	172 ± 35
		k_{cat} (s^{-1})	0.093 ± 0.005	0.100 ± 0.007
		k_{cat}/K_m (M^{-1}/s^{-1})	443 ± 136	580 ± 203

Nevertheless, the K_m values for INH were only subtly different between the WT-KatG protein and the variant (Table 1).

The K_m and k_{cat} values for NAD^+ of L333V-KatG were nearly identical to those of WT-KatG. IN-NAD formation in the absence of KatG was undetectable with the H_2O_2-generating G/Gox system (data not shown). This IN-NAD formation by WT-KatG was consistent with previously reported values [14].

Most of the catalytic effects found when comparing both enzymes are related to differences in both k_{cat} and K_m. The location of the L333V mutation suggests that the architecture of the active site and the distal residues are not affected. The loss of catalytic power could be due to a change in the arrangement of the residues below the heme group, affecting the redox potential of the enzyme (see below).

3.3. Thermal stability

Protein temperature unfolding was monitored by electronic circular dichroism at both 222 nm (monitoring the loss of ellipticity typical of α-helices) and 410 nm (monitoring the loss of ellipticity corresponding to the heme in its asymmetric environment at the active site). The data shown in Fig. 3 are normalized data measuring the apparent fraction of unfolded protein (Fapp).

A comparison of the thermal unfolding curves of the WT-KatG and L333V-KatG enzymes revealed significant differences. (Fig. 3A). L333V-KatG showed a loss of cooperativity in the denaturation mechanism, suggesting the presence of a folding intermediate, which has been observed with many other proteins including peroxidases. Loss of ellipticity at 222 nm started above 40 °C for WT-KatG while for L333V-KatG this happens at 37 °C, indicating that the mutation affected protein stability. The difference may be physiologically relevant since loss of structure is related to loss of function. The lack of cooperativity also has major implications *in vivo*. Thus, the KatG concentration required to form enough IN-NAD to inhibit InhA may not be achieved.

It is important to note that zero ellipticity values were never reached up to 60 °C, where a plateau was reached. The refolding process was irreversible, with only a slight increase in the CD signal at 222 nm. In fact, a comparison of the initial and final spectra when the L333V-KatG protein was returned to 20 °C showed significant differences with a loss of the two negative bands centered at 208 and 222 nm characteristic of the α-helical structure to a signal band centered at 115 nm characteristic of the β-structure (data not shown). On the other hand, although a significant amount of signal was lost, the WT-KatG spectra recorded after lowering the temperature resembled the helical characteristics. This

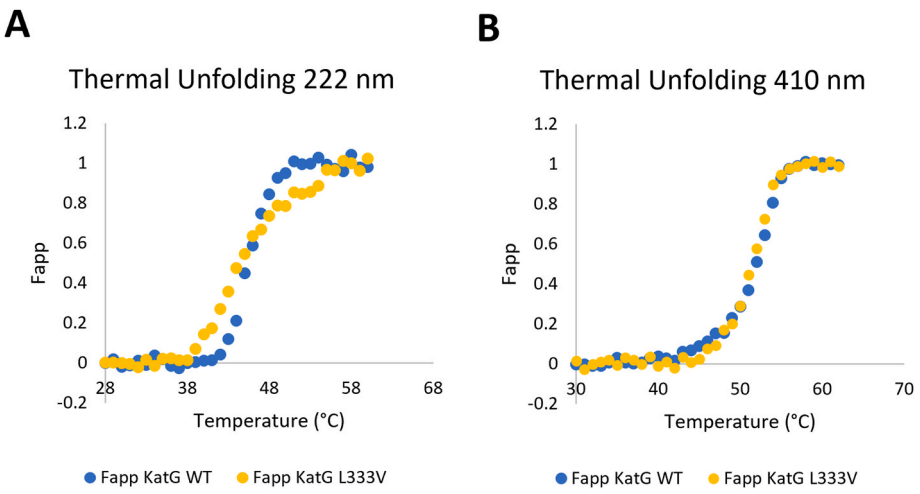

Fig. 3. Comparison of the thermal unfolding curves of the WT-KatG and L333V-KatG enzymes. A) In the far UV region (222 nm). B) Of the heme in the UV–Vis region (410 nm). Data shown are normalized the apparent fraction of unfolded protein (Fapp).

reflects the poor ability of the L333V-KatG to revert to its original structure compared to the WT-KatG enzyme, although this may be an effect caused solely by thermal denaturation.

By contrast, loss of heme ellipticity started above 45 °C, and between 53 and 55 °C more than 80% of the heme ellipticity was irreversibly lost (Fig. 3B). In the denatured state, the prosthetic group was completely released (no remaining ellipticity at 410 nm) in both proteins with no differences.

3.4. *Crystal structure of L333V-KatG*

The crystal asymmetric unit contains two L333V-KatG homodimers, chains A, B, C, and D please state which chains form the dimers, each including residues 24 to 740. Although the electronic density map for each monomer was mostly continuous, and its high quality clearly defined most of the main and side chains of residues, the densities for the N-terminal segment (residues 1–23) were not detected, probably due to high flexibility in this region; accordingly, these residues were not included in the model. Superposition of the two L333V-KatG dimers gave a root-mean-square deviation (RMSD) of 0.20 Å for the A and C subunits and 0.29 Å for the B and D subunits using 717 Cα atoms. Each dimer contains a heme *b* group, penta-coordinated sodium ions and water molecules, in addition to HEPES (4-(2-hydroxyethyl)-1-piperazineethanesulfonic acid) and triethylene glycol in different sites, present in the crystallization condition (Fig. 4A). This crystal structure departs only locally from WT-KatG (PDB ID 2CCA), with a RMSD of 0.37 Å for the A subunits and 0.39 Å for the B subunits using 714 Cα atoms.

Regarding the arrangement of catalytically important residues surrounding the heme, it is practically the same as that in the WT-KatG enzyme (PDB ID 2CCA) and other catalase-peroxidases [5,6,16,17]. In addition, the electronic density map (2*Fo-Fc*) clearly describes the architecture of the heme-containing active site, fully occupied and unmodified. The proximal (H270, W321, and D381) and distal (R104, W107, and H108) triads are found at almost identical positions, as is the KatG-typical covalent adduct M255-Y229-W107 (Figs. 4B and 5A).

However, the organization of the water molecules is very different in the L333V-KatG structure. In WT-KatG there are four well-ordered water molecules above the heme, within the distal pocket of the protein, that are not conserved in our structure. In particular, the structural water molecule that is coordinated with the heme iron was not observed in L333V-KatG; this could be due to the formation of the oxygen adduct with W107 (see below). Furthermore, L333V-KatG contains two additional water molecules (Fig. 5A and Supplementary Fig. S1A) which are also observed in *Bp*-KatG [30] (Supplementary Fig. S1B).

L333V-KatG has a perhydroxy modification of the indole nitrogen atom of W107 (Figs. 4B and 5A); such modification was reported for W111 in the *Bp*-KatG (PDB ID 5L02, S324T variant) [30] (Supplementary Fig. S1B), in *Magnaporthe grisea* KatG [12] and *Neurospora crassa* CAT-2 [31] but is absent in WT-KatG. The W107 perhydroxy is at a distance of 2.7 Å from the heme iron (Supplementary Fig. S1A). An

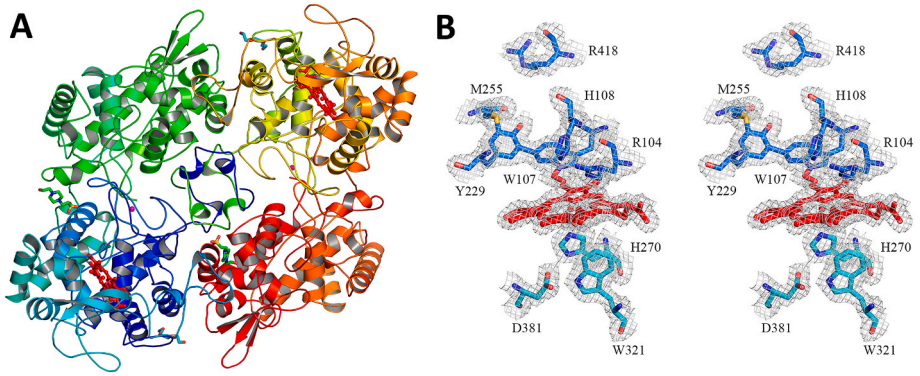

Fig. 4. L333V-KatG homodimer (chains A and B) and active site structures. A) Each subunit N-terminal domain contains heme (PDB ID 8DWR). Ligands are also shown: HEPES (green sticks), triethylene glycol (cyan sticks) and sodium ions (purple spheres). B) Stereo view (cross-eye) of the active site with its electronic density map (2*Fo-Fc*). Shown are the proximal (H270, W321, and D381 in cyan) and distal (R104, W107, and H108 in blue) triads, the covalent adduct M255-Y229-W107, and the mobile R418. (For interpretation of the references to colour in this figure legend, the reader is referred to the Web version of this article.)

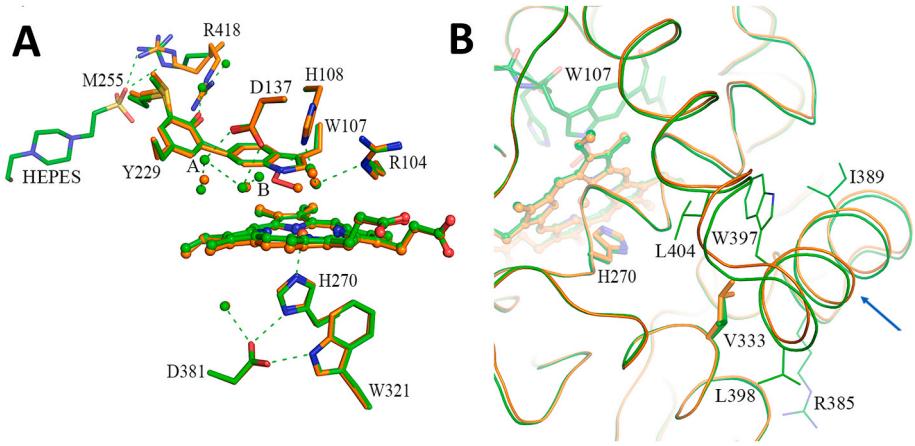

Fig. 5. Structural comparison of L333V-KatG with WT-KatG. A) L333V-KatG (green) active site in superposition with WT-KatG (orange, PDB ID 2CCA) active site. Essential amino acids for catalase and peroxidase activities are indicated. Compared with WT-KatG, L333V-KatG has two more water molecules at the active site marked as A and B, and R418 in the R conformation makes two hydrogen bonds with a HEPES molecule. B) Superposition of L333V-KatG with WT-KatG showing mutation L333V and the movement of the helix segment comprising R385 to L404 (marked with a blue arrow). Other amino acid residues are indicated as reference. (For interpretation of the references to colour in this figure legend, the reader is referred to the Web version of this article.)

adduct radical has been reported in the reaction of KatGs with molecular oxygen to form the perhydroxy modification on the adduct tryptophan indole [9,32].

The segment from R385 to L404 shifted, moving towards the mutation V333 by 0.4–0.8 Å. This shift is due to the mutation L333V, since valine has a smaller side chain than leucine, which could change some hydrophobic packing interactions around V333 (Fig. 5B).

A notable difference occurs in the bond length between H270 and heme Fe, which is longer in L333V-KatG (2.6 Å) with respect to WT-KatG (2.2 Å) (Supplementary Fig. S2). This could be reason enough to have a significantly weaker bond, and thus the heme would be released more easily. The MetalPDB database (March 2023) has information of all PDB records that have metals and analyses of the binding sites. For heme groups, typical Fe–N distances (with N contributed by His) are mostly below 2.25 Å. For L333V-KatG the distance is out of the ordinary range. H270 and W321 engage in hydrogen bonds with D381 (Fig. 5A); while the bond length between H270 and D381 is similar in WT-KatG and L333V-KatG (2.81–2.82 Å and 2.62–2.82 Å, respectively), the bond to W321 is longer in L333V-KatG (2.52–2.57 Å and 2.60–2.78 Å, respectively). Given that W321 stacks perpendicular to the heme group, longer hydrogen bonds could affect the electronic distribution on both W321 and the heme. The connection to position 333 is through F332, as this aromatic residue has Van der Waals interactions with L/V333, H270, D381, and W321. Modifications in the electronic distribution at the heme are likely to result in changes in the redox potential of the Fe (see next section) and could be related to the decrease in k_{cat} by H_2O_2 and *O*-dianisidine of L333V-KatG compared to WT-KatG (Table 1).

Another potential difference in L333V-KatG in comparison with WT-KatG is the probable presence of a sodium ion found in each L333V-KatG subunit. This sodium ion is supported by its electronic density and pentavalent coordination structure (Fig. 4A and Supplementary Fig. S3A). This sodium ion in *M. tuberculosis* KatG had not been reported before. The buffer in which L333V-KatG was crystallized contained sodium. The sodium ion is bound to the main chain oxygen of G118, the main chain oxygen of G120, the side chain oxygen of S486 and two water molecules. A sodium ion has also been reported in *Bp*-KatG [33] (Supplementary Fig. S3B) and *Se*-KatG [16], and a potassium ion in *N. crassa* CAT-2 in a conserved location as sodium ion [31].

It was interesting to see that R418, which has been postulated to act as a molecular switch modulating the redox properties of the MYW adduct, is present in only one conformation which is not interacting with Y229, although it is unclear if this is due to the L333V modification or to the crystallization conditions. The residues from the adduct and the mobile arginine have been shown to be essential for the catalase activity but not for the peroxidase reaction [34]. The lack of interaction between Y229 and D418 seems to be due to the presence of a HEPES molecule, with which D418 forms two hydrogen bonds in chains A and C in L333V-KatG (Fig. 5A). This HEPES binding site did not match with any of the isoniazid binding sites described in KatGs [4,16]. However, where mobile arginine is found, it could be a binding site. Analysis of this mobile arginine in other prokaryotic KatG deposited in the PBD [11] shows that it is found in two conformations (Y and R), where R points away from the adduct, toward another conserved arginine, the conformations depending on the pH of crystallization and the oxidation state of the heme. Another structural feature of the Y conformation of mobile arginine is the covalent modification of the indole nitrogen of the tryptophan adduct. In our structure, W107 exhibits a perhydroxy modification that is consistent with the pH used in crystallization (pH 7.5).

3.5. Electrochemical properties

The changes in the redox potential of the heme group were studied by electrochemical techniques. The Supplementary Fig. S4 shows the CV responses of WT-KatG and L333V-KatG in the elution buffer electrolytic solution. The redox processes associated with the Fe^{3+}/Fe^{2+} pair of the heme group appear between 0 and 0.2 V. Upon reduction, the cyclic voltammograms for WT-KatG and L333V-KatG display irreversible cathodic peaks with maxima at 0.169 and 0.139 V versus SHE, respectively. WT-KatG exhibits a peak with an E0' of 0.214 V, while L333V-KatG exhibits a peak centered at 0.139 V versus the SHE (Supplementary Fig. S4B). The electrochemical results indicate that the L333V-KatG variant affected the redox behavior of the heme group, consistent with a reduction in catalytic activity (Table 1). Details on the interpretation of these measurements are given in the supplementary file.

4. Conclusions

The analysis presented in this study contributes to a more comprehensive description of the complex structure-function relationships in INH-resistance derived from KatG activity. The observations made with the L333V-KatG and WT-KatG revealed *in vitro* activities of catalase, peroxidase and IN-NAD formation (in the presence of H_2O_2) at different rates, which could relate to the INH resistance. On the other hand, the resistance could occur through distinct mechanisms, consistent with the observation that L333V-KatG is less stable than the WT-KatG, which may

result in limited activity of this variant *in vivo*. The L333-KatG structure solved here reveals the presence of a perhydroxy modification of the indole nitrogen atom of W107, the movement of segment R385 to L404, and the change in bond length between H270 and heme Fe, which is longer in L333V-KatG (2.6 Å) than in WT-KatG (2.2 Å), resulting in a smaller redox potential for L333V-KatG. Some of these differences may be relevant to the mechanism of INH resistance in this and other KatG mutant enzymes.

CRediT authorship contribution statement

Brenda Uribe-Vázquez: Data curation, Investigation, Methodology, Project administration, Writing – original draft, Writing – review & editing, Formal analysis. **Adelaida Díaz-Vilchis:** Formal analysis, Investigation, Methodology, Writing – original draft, Writing – review & editing. **Aylin Avila-Linares:** Methodology. **Gloria Saab-Rincón:** Conceptualization, Data curation, Validation, Writing – review & editing. **Yerli Marín-Tovar:** Data curation, Visualization. **Humberto Flores:** Methodology, Writing – review & editing. **Nina Pastor:** Validation, Writing – review & editing. **Guillermo Huerta-Miranda:** Data curation. **Enrique Rudiño-Piñera:** Supervision. **Xavier Soberón:** Supervision, Writing – original draft, Writing – review & editing.

Declaration of competing interest

The authors declare no potential competing interests.

Data availability

Data will be made available on request.

Acknowledgements

BUV received a PhD grant CVU 672126 given by CONACYT, México. ERP and XS received financial support from institutional budget from IBt, UNAM. We acknowledge to the National Institute of Genomic Medicine and National Institute of Respiratory Disease, México, for DNA donating. We also acknowledge Lilian González Segura for assistance in data collection. Crystallographic results shown in this report are derived from work performed at Argonne National Laboratory, Structural Biology Center at the Advanced Photon Source, operated by UChicago Argonne, LLC, for the U.S. Department of Energy, Office of Biological and Environmental Research under contract DE-AC02-06CH11357.

Appendix A. Supplementary data

Supplementary data to this article can be found online at https://doi.org/10.1016/j.bbrep.2024.101649.

References

[1] WHO, Global Tuberculosis Report 2019 *Global tuberculosis Report*, 2020, p. 201.
[2] C.E. Cade, A.C. Dlouhy, K.F. Medzihradszky, S.P. Salas-Castillo, R.A. Ghiladi, Isoniazid-resistance conferring mutations in *Mycobacterium tuberculosis* KatG: catalase, peroxidase, and INH-NADH adduct formation activities, Protein Sci. 19 (3) (2010) 458–474, https://doi.org/10.1002/pro.324.
[3] O.J. Njuma, E.N. Ndontsa, D.C. Goodwin, Catalase in peroxidase clothing: interdependent cooperation of two cofactors in the catalytic versatility of KatG, Arch. Biochem. Biophys. 544 (2014) 27–39, https://doi.org/10.1016/j.abb.2013.11.007.
[4] B. Wiseman, X. Carpena, M. Feliz, L.J. Donald, M. Pons, I. Fita, et al., Isonicotinic acid hydrazide conversion to Isonicotinyl-NAD by catalase-peroxidases, J. Biol. Chem. 285 (34) (2010) 26662–26673, https://doi.org/10.1074/jbc.M110.139428.
[5] X. Zhao, H. Yu, S. Yu, F. Wang, J.C. Sacchettini, R.S. Magliozzo, Hydrogen peroxide-mediated isoniazid activation catalyzed by *Mycobacterium tuberculosis* catalase-peroxidase (KatG) and its S315T mutant, Biochemistry 45 (13) (2006) 4131–4140, https://doi.org/10.1021/bi051967o.
[6] T. Bertrand, N.A. Eady, J.N. Jones, J.M. Jesmin Nagy, B. Jamart-Gregoire, et al., Crystal structure of *Mycobacterium tuberculosis* catalase-peroxidase, J. Biol. Chem. 279 (37) (2004) 38991–38999, https://doi.org/10.1074/jbc.M402382200.
[7] M. Machuqueiro, B. Victor, J. Switala, J. Villanueva, C. Rovira, I. Fita, et al., The catalase activity of catalase-peroxidases is modulated by changes in the pKa of the distal histidine, Biochemistry 56 (17) (2017) 2271–2281, https://doi.org/10.1021/acs.biochem.6b01276.
[8] J. Colin, B. Wiseman, J. Switala, P.C. Loewen, A. Ivancich, Distinct role of specific tryptophans in facilitating electron transfer or as [Fe(IV)=O Trp(*)] intermediates in the peroxidase reaction of *Bulkholderia pseudomallei* catalase-peroxidase: a multifrequency EPR spectroscopy investigation, J. Am. Chem. Soc. 131 (24) (2009) 8557–8563, https://doi.org/10.1021/ja901402v.
[9] A. Díaz, P.C. Loewen, I. Fita, X. Carpena, Thirty years of heme catalases structural biology, Arch. Biochem. Biophys. 525 (2012) 102–110, https://doi.org/10.1016/j.abb.2011.12.011.
[10] M. Zamocky, P.G. Furtmuller, C. Obinger, Evolution of structure and function of Class I peroxidases, Arch. Biochem. Biophys. 500 (1) (2010) 45–57, https://doi.org/10.1016/j.abb.2010.03.024.
[11] O.J. Njuma, I. Davis, E.N. Ndontsa, J.R. Krewall, A. Liu, D.C. Goodwin, Mutual synergy between catalase and peroxidase activities of the bifunctional enzyme KatG is facilitated by electron hole-hopping within the enzyme, J. Biol. Chem. 292 (45) (2017) 18408–18421, https://doi.org/10.1074/jbc.M117.791202.
[12] M. Zamocky, Q. Garcia-Fernandez, B. Gasselhuber, C. Jakopitsch, P.G. Furtmüller, P.C. Loewen, I. Fita, C. Obinger, X. Carpena, High conformational stability of secreted eukaryotic catalase-peroxidases: answers from first crystal structure and unfolding studies, J. Biol. Chem. 287 (2012) 32254–32262, https://doi.org/10.1074/jbc.M112.384271.
[13] CryPTIC, Comprehensive Resistance Prediction for Tuberculosis: an International Consortium Retrieved Enero, 2020, 2020, http://www.crypticproject.org/.
[14] F. Brossier, M. Boudinet, V. Jarlier, S. Petrella, W. Sougakoff, Comparative study of enzymatic activities of new KatG mutants from low- and high-level isoniazid-resistant clinical isolates of *Mycobacterium tuberculosis*, Tuberculosis 100 (2016) 15–24, https://doi.org/10.1016/j.tube.2016.06.002.
[15] M.V. Bertacine, I. Bordin, A.M. Xavier, V. Fadel, L. Augusto, W. Filgueira de Azevedo, D. Santiago, Crystallographic studies on the binding of isonicotinyl-NAD adduct to wild-type and isoniazid resistant 2-trans-enoyl-ACP (CoA) reductase from *Mycobacterium tuberculosis*, J. Struct. Biol. 159 (2007) 1047–8477, https://doi.org/10.1016/j.jsb.2007.04.009.
[16] S. Kamachi, K. Hirabayashi, M. Tamoi, S. Shigeoka, T. Tada, K. Wada, The crystal structure of isoniazid-bound KatG catalase-peroxidase from *Synechococcus elongatus* PCC7942, FEBS J. 282 (1) (2015) 54–64, https://doi.org/10.1111/febs.13102.
[17] A. Munir, M.T. Wilson, S.W. Hardwick, D.Y. Chirgadze, J.A.R. Worrall, T. L. Blundell, A.K. Chaplin, Using cryo-EM to understand antimycobacterial resistance in the catalase-peroxidase (KatG) from, Mycobacterium tuberculosis, Structure 29 (Issue 8) (2021) 899–912.e4, 2021.
[18] D.M. Juarez-Eusebio, D. Munro-Rojas, R. Muñiz-Salazar, R. Laniado-Laborín, J. A. Martinez-Guarneros, C.A. Flores-López, R. Zenteno-Cuevas, Molecular characterization of multidrug-resistant *Mycobacterium tuberculosis* isolates from high prevalence tuberculosis states in Mexico, Infect. Genet. Evol. 55 (2017) 384–391, https://doi.org/10.1016/j.meegid.2016.09.012, 2017 Nov.
[19] G. Sarkar, S.S. Sommer, The "megaprimer" method of site-directed mutagenesis, Biotechniques 8 (4) (1990) 404–407. PMID: 2340178.
[20] C.J. Wei, B. Lei, J.M. Musser, S.C. Tu, Isoniazid activation defects in recombinant *Mycobacterium tuberculosis* catalase-peroxidase (KatG) mutants evident in InhA inhibitor production, Antimicrob. Agents Chemother. 47 (2) (2003) 670–675, https://doi.org/10.1128/AAC.47.2.670-675.2003.
[21] W. Kabsch, Integration, scaling, space-group assignment and post-refinement, Acta Crystallogr. D Biol. Crystallogr 66 (2010) 125–132, https://doi.org/10.1107/S0907444909047374.
[22] A.J. McCoy, R.W. Grosse-Kunstleve, P.D. Adams, M.D. Winn, L.C. Storoni, R. J. Read, Phaser crystallographic software, J. Appl. Crystallogr. 40 (2007) 658–674, https://doi.org/10.1107/S0021889807021206.
[23] G.N. Murshudov, A.A. Vagin, E.J. Dodson, Refinement of macromolecular structures by the maximum-likelihood method, Acta Crystallogr. D: Biol. Crystallogr 53 (1997) 240–255, https://doi.org/10.1107/S0907444996012255.
[24] P.D. Adams, P.V. Afonine, G. Bunkóczi, V.B. Chen, I.W. Davis, N. Echols, J. J. Headd, L.W. Hung, G.J. Kapral, R.W. Grosse-Kunstleve, A.J. McCoy, N. W. Moriarty, R. Oeffner, R.J. Read, D.C. Richardson, et al., PHENIX: a comprehensive Python-based system for macromolecular structure solution, Acta Crystallogr. D Biol. Crystallogr 66 (2010) 213–221, https://doi.org/10.1107/S0907444909052925.
[25] P. Emsley, B. Lohkamp, W.G. Scott, K. Cowtan, Features and development of coot, Acta Crystallogr. D Biol. Crystallogr 66 (2010) 486–501, https://doi.org/10.1107/S0907444910007493.
[26] V.B. Chen, W.B. Arendall, J.J. Headd, D.A. Keedy, R.M. Immormino, G.J. Kapral, L. W. Murray, J.S. Richardson, D.C. Richardson, MolProbity: all-atom structure validation for macromolecular crystallography, Acta Crystallogr. D Biol. Crystallogr 66 (2010) 12–21, https://doi.org/10.1107/S0907444909042073.
[27] K. Johnsson, W.A. Froland, P.G. Schultz, Overexpression, purification, and characterization of the catalase-peroxidase KatG from *Mycobacterium tuberculosis*, J. Biol. Chem. 272 (5) (1997) 2834–2840.
[28] J.M. Nagy, A.E. Cass, K.A. Brown, Purification and characterization of recombinant catalase-peroxidase, which confers isoniazid sensitivity in *Mycobacterium tuberculosis*, J. Biol. Chem. 272 (50) (1997) 31265–31271.
[29] B. Saint-Joanis, H. Souchon, M. Wilming, K. Johnsson, P.M. Alzari, S.T. Cole, Use of site-directed mutagenesis to probe the structure, function and isoniazid activation of the catalase/peroxidase, KatG, from *Mycobacterium tuberculosis*, Biochem. J. 338 (1999) 753–760, https://doi.org/10.1042/0264-6021:3380753.

[30] T. Deemagarn, X. Carpena, R. Singh, B. Wiseman, I. Fita, P.C. Loewen, Structural characterization of the Ser324Thr variant of the catalase-peroxidase (KatG) from *Burkholderia pseudomallei*, J. Mol. Biol. 345 (2005) 21–28, https://doi.org/10.1016/j.jmb.2004.10.020.

[31] V. Vega-García, A. Díaz-Vilchis, J.P. Saucedo-Vázquez, A. Solano-Peralta, E. Rudiño-Piñera, W. Hansberg, Structure, kinetics, molecular and redox properties of a cytosolic and developmentally regulated fungal catalase-peroxidase, Arch. Biochem. Biophys. 15 (640) (2018) 17–26, https://doi.org/10.1016/j.abb.2017.12.021. Epub 2018 Jan 2. PMID: 29305053.

[32] P. Vidossich, P.C. Loewen, I. Fita, C. Rovira, Oxygen binding to catalase-peroxidase, J. Phys. Chem. Lett. 2 (2011) 196–200, https://doi.org/10.1021/jz1015795.

[33] X. Carpena, S. Loprasert, S. Mongkolsuk, J. Switala, P.C. Loewen, I. Fita, Catalase-peroxidase KatG of *Burkholderia pseudomallei* at 1.7A resolution, J. Mol. Biol. 327 (2003) 475–489, https://doi.org/10.1016/s0022-2836(03)00122-0.

[34] G. Smulevich, C. Jakopitsch, E. Droghetti, C. Obinger, Probing the structure and bifunctionality of catalase-peroxidase (KatG), J. Inorg. Biochem. 100 (2006) 568–585, https://doi.org/10.1016/j.jinorgbio.2006.01.033.